

Investigation of aqueous alcohol and sugar solutions with reflection terahertz time-domain spectroscopy

Peter Uhd Jepsen,¹ Uffe Møller¹ and Hannes Merbold²

¹COM•DTU - Department of Communications, Optics and Materials, Technical University of Denmark, DK-2800 Kongens Lyngby, Denmark

²Department of Molecular and Optical Physics, Institute of Mathematics and Physics, University of Freiburg, D-79104 Freiburg, Germany

jepsen@com.dtu.dk

Abstract: We give a detailed analysis of a general realization of reflection terahertz time-domain spectroscopy. The method is self-referenced and applicable at all incidence angles and for all polarizations of the incident terahertz radiation. Hence it is a general method for the determination of the dielectric properties of especially liquids in environments where transmission measurements are difficult. We investigate the dielectric properties in the 0.1-1.0 THz frequency range of liquids using reflection terahertz time-domain spectroscopy. We apply the technique for the determination of alcohol and sugar concentration of commercial alcoholic beverages and liquors. The special geometry of the experiment allows measurement on sparkling beverages.

© 2007 Optical Society of America

OCIS codes: (300.6495) Spectroscopy, terahertz; (220.2740) Geometric optical design; (120.4825) Optical time-domain reflectometry

References and links

1. L. Thrane, R. H. Jacobsen, P. Uhd Jepsen, and S. R. Keiding, "THz reflection spectroscopy of liquid water," *Chem. Phys. Lett.* **240**, 330 (1995)
2. C. Rønne, L. Thrane, P.-O. Åstrand, A. Wallqvist, K. V. Mikkelsen, and S. R. Keiding, "Investigation of the temperature dependence of dielectric relaxation in liquid water by THz reflection spectroscopy and molecular dynamics simulation," *J. Chem. Phys.* **107**, 5319 (1997)
3. J. Dai, J. Zhang, W. Zhang, and D. Grischkowsky, "Terahertz time-domain spectroscopy characterization of the far-infrared absorption and index of refraction of high-resistivity, float-zone silicon," *J. Opt. Soc. Am. B* **21**, 1379 (2004)
4. D. Grischkowsky, S. Keiding, M. van Exter, and Ch. Fattiger, "Far-infrared time-domain spectroscopy with terahertz beams of dielectrics and semiconductors," *J. Opt. Soc. Am. B* **7**, 2006 (1990)
5. H. Hirori, K. Yamashita, M. Nagai, and K. Tanaka, "Attenuated total reflection spectroscopy in time domain using terahertz coherent pulses," *Jpn. J. Appl. Phys.* **43**, L1287 (2004)
6. A. Dobriu, R. Beigang, C. Otani, and K. Kawase, "Monolithic Fabry-Perot resonator for the measurement of optical constants in the terahertz range," *Appl. Phys. Lett.* **86**, 261107 (2005)
7. P. Uhd Jepsen and B. M. Fischer, "Dynamic range in terahertz time-domain transmission and reflection spectroscopy," *Opt. Lett.* **30**, 29 (2005)
8. T.-I. Jeon and D. Grischkowsky, "Characterization of optically dense, doped semiconductors by reflection THz time domain spectroscopy," *Appl. Phys. Lett.* **72**, 3032 (1998)
9. C. Rønne, *Intermolecular liquid dynamics studied by THz-spectroscopy*, Ph.D. Thesis, Aarhus University (2000)
10. J. Barthel, K. Bachhuber, R. Buchner, and H. Hetzenauer, "Dielectric spectra of some common solvents in the microwave region. Water and lower alcohols," *Chem. Phys. Lett.* **165**, 369 (1990)

11. J. T. Kindt and C. A. Schmuttenmaer, "Far-infrared dielectric properties of polar liquids probed by femtosecond terahertz pulse spectroscopy," *J. Phys. Chem.* **100**, 10373 (1996)
 12. H. Kitahara, T. Yagi, K. Mano, M. Wada Takeda, S. Kojima, and S. Nishizawa, "Dielectric characteristics of water solutions of ethanol in the terahertz region," *J. Korean Phys. Soc.* **46**, 82 (2005)
 13. M. Nagel, M. Först, and H. Kurz, "THz biosensing devices: fundamentals and technology," *J. Phys. Condens. Matter* **18**, S601 (2006)
 14. P. Uhd Jepsen, R. H. Jacobsen, and S. R. Keiding, "Generation and detection of terahertz pulses from biased semiconductor antennas," *J. Opt. Soc. Am. B* **13**, 2424 (1996)
 15. L. Duvillaret, F. Garet, and J.-L. Coutaz, "A reliable method for extraction of material parameters in terahertz time-domain spectroscopy," *IEEE J. Sel. Top. Quantum Electron.* **2**, 739 (1996)
 16. T. Tassaing, Y. Dantan, M. Besnard, E. Zoidis, and J. Yarwood, "A far infrared study of benzene-fluorinated benzene binary mixtures," *Chem. Phys.* **184**, 225 (1994)
 17. B. N. Flanders, R. A. Cheville, D. Grischkowsky, and N. F. Scherer, "Pulsed terahertz transmission spectroscopy of liquid CHCl_3 , CCl_4 , and their mixtures," *J. Phys. Chem.* **100**, 11824 (1996)
 18. D. S. Venables, A. Chiu, and C. A. Schmuttenmaer, "Structure and dynamics of nonaqueous mixtures of dipolar liquids. I. Infrared and far-infrared spectroscopy," *J. Chem. Phys.* **113**, 3243 (2000)
 19. D. S. Venables and C. A. Schmuttenmaer, "Spectroscopy and dynamics of mixtures of water with acetone, acetonitrile, and methanol," *J. Chem. Phys.* **113**, 11222 (2000)
-

1. Introduction

Terahertz time-domain spectroscopy (THz-TDS) is a method for the determination of the real and imaginary part of the dielectric function, or the absorption coefficient and index of refraction. This method has found extended use in a wide range of research fields, including studies of carrier dynamics in semiconductors, low-frequency vibrational modes in molecular crystals, and low-energy interactions in polar and nonpolar liquids.

THz-TDS can be performed both as a transmission measurement and as a reflection measurement. The transmission geometry is easiest to implement, and the majority of data reported in the literature has been obtained with transmission setups. However, since THz-TDS is a phase-sensitive technique a determination of the complex reflection coefficient of a sample by reflection spectroscopy yields the equivalent information about the dielectric function of the sample. Reflection THz-TDS has earlier been used for investigations of the temperature dependence of the dielectric properties of water [1, 2], and recently Hirori *et al.* used attenuated total internal reflection THz-TDS to study the optical properties of semiconductor materials and liquid water [5]. Dubroiu *et al.* have shown that the loss factor of a monolithic Fabry-Perot resonator is modified by sample material in contact with the total internal reflection facet of the resonator, and that this mechanism can be used to determine the alcohol content in aqueous solutions [6]. The dynamic range and noise limitations in transmission and reflection THz-TDS measurements were investigated by Jepsen and Fischer [7].

Both transmission- and reflection spectroscopy requires a reference spectrum, recorded under known conditions, in order to extract quantitative information about the dielectric function of a sample. In transmission spectroscopy this reference measurement is typically recorded without a sample in the beam path, or by varying the thickness of a liquid sample. Since both the reference- and sample signal shapes depend on both spectrometer alignment and the generation- and detection process, a reference signal is preferably recorded for each measurement, hence doubling the required data acquisition time. In reflection spectroscopy, the reference signal can be recorded by replacing the sample with a known reflector, for instance a metal mirror. This approach is very sensitive to the precise placement of the reference mirror with respect to the sample surface, and in practice, some compensation in the analysis is required [8]. Another method, which eliminates the need to replace the sample surface with a metal mirror, was described by Thrane *et al.* [1], who placed the sample, in that case water, in contact with a thick silicon window. In this geometry both the reference- and the sample signals are available in a single recording, obtained as the reflection from the air/silicon interface and the silicon/sample

interface, respectively. The normal incidence of the THz signal onto the window requires an experimental setup which includes a beamsplitter in the THz beam path, and hence the detected signal is reduced significantly in amplitude. This complication can be avoided by choosing a non-normal incidence angle, at the expense of complicating the procedure for extraction of the dielectric function of the sample material. Rønne treated this problem, and described an iterative process for the calculation of the dielectric function [9].

Inspired by that work we derive here expressions that can be used for the calculation of the dielectric function of a sample material in contact with a transparent window material such as silicon, without limitations to the incidence angle and polarization state of the incident THz field. This analysis is crucial for the correct evaluation of quantitative spectroscopic results from THz reflection spectrometers. Since this method records both the reference- and the sample signals in the same scan, it may be referred to as self-referenced reflection THz time-domain spectroscopy.

Following the discussion of the analysis of the reflection spectroscopy, we will illustrate its applicability in the characterization of the dielectric properties of water-ethanol mixtures, and in particular we will present a method for the determination of the alcohol concentration in commercial beverages and liquors, independent of the presence of other components such as flavor, color, organic precipitates, as well as carbonation of the beverage. We will also investigate the influence of higher concentrations of sugar in the solutions, and finally demonstrate that the method can be used for the simultaneous determination of both alcohol- and sugar concentration in a solution.

2. Self-referenced THz reflection spectroscopy

In this section we will describe the method for extraction of the dielectric function in a reflection setup, in the general situation with arbitrary incidence angle as well as arbitrary incident polarization angle of the electric field.

2.1. Full analysis

The reflection coefficient is most conveniently defined for the two orthogonal components of the electric field *parallel* to the incidence plane of the sample window and *perpendicular* to the incidence plane of the sample window. In the general case the polarization of the electric field may have any angle with respect to the incidence plane. The polarization may also be circular or elliptical. The spectrometer layout that we will describe in the following features linear polarization of the incident electric field. Typical pulsed THz emitters, such as photoconductive dipole antennas and electro-optic crystals, normally generate linearly polarized radiation. The state of the polarization throughout the spectrometer is then defined by the geometrical arrangement of the mirrors that control the beam path. Any out-of-plane reflection of the THz beam in the spectrometer will lead to a rotation of the polarization. In addition, any differences in the reflection coefficients between *s*- and *p*-polarized light at reflective surfaces in the spectrometer will also modify the state of polarization of the light.

The optical path of the THz beam inside our spectrometer is illustrated in Fig. 1.

This particular geometry is based on a standard transmission spectrometer with an intermediate focus. In this geometry the THz beam is guided and focused by off-axis paraboloidal mirrors with equal effective focal lengths f . The mirrors are placed in a $f - 2f - f$ geometry both before and after the intermediate focus. The incidence planes of these mirrors are shown as gray rectangles in Fig. 1. This arrangement ensures a 1:1 imaging of the emitter plane onto the sample window and further onto the detector. The four off-axis paraboloidal mirrors and the THz emitter and detector all lie in the same plane, which we will denote the main plane of the spectrometer. The beam path is indicated by the red lines in Fig. 1.

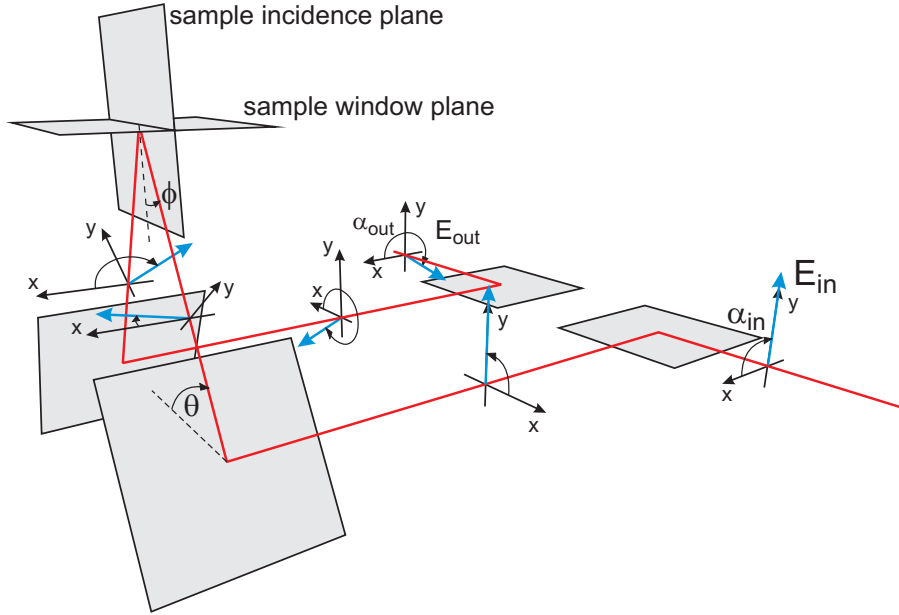


Fig. 1. Beam path of the reflection spectrometer. The gray rectangles indicate the incidence planes of the four off-axis paraboloidal mirrors. The sample window is elevated from the main plane of the spectrometer by rotation of the incidence planes before and after the sample. The vectors shown in blue color illustrate the polarization of an initially vertically polarized THz field through the spectrometer.

The reflection geometry is realized by elevating the sample plane out of the main plane of the spectrometer, to a height h by rotation of the off-axis paraboloidal mirrors before and after the sample. This done in a manner that preserves the distances f from the sample surface to the two rotated mirrors. We have used an elevation angle $\theta = 60^\circ$, as indicated in Fig. 1. This means that the angle of incidence on the sample window is $\phi = 30^\circ$.

We can follow the polarization through the spectrometer by application of the Jones matrix formalism. Here it is useful to recall that in the principal coordinate system of the reflection plane, the polarization vector is changed according to

$$\begin{pmatrix} E'_{\parallel} \\ E'_{\perp} \end{pmatrix} = \begin{pmatrix} -r_{\parallel} & 0 \\ 0 & r_{\perp} \end{pmatrix} \begin{pmatrix} E_{\parallel} \\ E_{\perp} \end{pmatrix}, \quad (1)$$

where the negative sign on r_{\parallel} describes the geometrical mirroring of the polarization vector in the plane perpendicular to the incidence plane. For most metals at THz frequencies, the reflection coefficients $r_{\parallel} \approx -1$ and $r_{\perp} \approx -1$. In a system with several reflective surfaces, the beam may be directed out of the incidence plane of the previous mirror. This is the case in the spectrometer described here. The polarization change is easiest described in the principal coordinate system of each new incidence plane. The transformation to this coordinate system from the previous incidence plane is described by the rotation matrix

$$M(\theta) = \begin{pmatrix} \cos \theta & \sin \theta \\ -\sin \theta & \cos \theta \end{pmatrix}, \quad (2)$$

where θ is the rotation angle of the current incidence plane with respect to that of the previous reflection.

Using this standard formalism we can determine the polarization of the incident THz field in the incidence plane of the sample window, and determine the THz polarization state at the THz detector. In the specific situation described here, the THz beam is reflected at an angle $\theta = 60$ degrees out of the plane. The polarization of the THz beam in the detector plane is then $\alpha' = 180^\circ + 2\theta - \alpha$, where α is the polarization angle of the input THz field, with respect to horizontal. The polarization is traced through our spectrometer as represented by the blue vectors in Fig. 1.

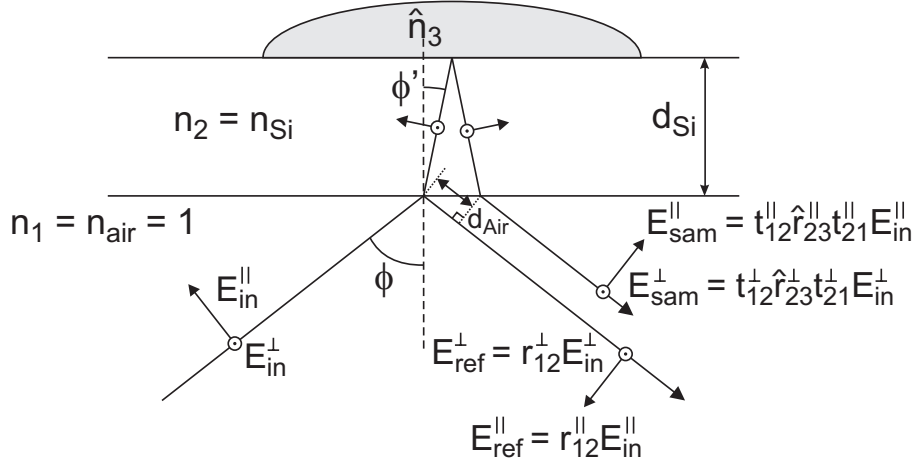


Fig. 2. Detailed view of the reflection geometry at the window which splits the input THz signal into a reference part and a sample part.

In addition to the geometrical rotation of the polarization rotation, the different reflection coefficients of the *s*- and *p*-components of the field at the sample window will lead to an additional phase retardation between the two components of the polarization in that reflection plane. General expressions for the two electric field components at the output plane of the spectrometer can be derived for arbitrary input polarizations, and for arbitrary geometries of the beam path in the spectrometer.

The window material should have known dielectric properties. High-purity silicon has a constant index of refraction of 3.425 and negligible absorption at room temperature in the spectral range relevant for this work [2]. More recent work [3] has reported a very precise value of 3.4175, in line with the first THz-TDS characterization of crystalline silicon [4], which reported a value of 3.4177 at room temperature.

The high index of refraction is ideal for the purpose since it results in a normal-incidence field reflection coefficient of -0.54. This gives a good balance between the signal strength of the reference reflection and the sample reflection.

The known dielectric properties of the window material can be used to solve an important problem in the experimental geometry. As indicated in Fig. 2 the sample beam is displaced slightly with respect to the reference beam after propagation through the window material. This will influence the shape of the detected sample signal since the coupling to the detector antenna will be different if the propagation axis is not identical to that of the reference signal. This effect is difficult to take into account in a strictly formal manner, but nevertheless the effect of the displacement can be taken into account in a more empirical way [9], by imposing an additional frequency-dependent amplitude calibration factor $A_{\text{cal}}(\omega)$ and phase shift $\Delta_{\text{cal}}(\omega)$ to the sample signal.

The components of the electric field at the output plane are then

$$\vec{E}_{out}^{ref} = \frac{1}{2} E_{in} \begin{pmatrix} (r_{12}^{\parallel} - r_{12}^{\perp}) \cos \alpha - (r_{12}^{\parallel} + r_{12}^{\perp}) \cos(\alpha - 2\theta) \\ (r_{12}^{\parallel} - r_{12}^{\perp}) \sin \alpha + (r_{12}^{\parallel} + r_{12}^{\perp}) \sin(\alpha - 2\theta) \end{pmatrix}, \quad (3)$$

$$\begin{aligned} \vec{E}_{out}^{sam} &= \frac{1}{2} E_{in} A_{cal} \exp(i\Delta_{cal}) \exp(2in_2\omega d_{eff}/c) \\ &\times \begin{pmatrix} (\hat{r}_{23}^{\parallel} t_{12}^{\parallel} t_{21}^{\parallel} - \hat{r}_{23}^{\perp} t_{12}^{\perp} t_{21}^{\perp}) \cos \alpha - (\hat{r}_{23}^{\parallel} t_{12}^{\parallel} t_{21}^{\parallel} + \hat{r}_{23}^{\perp} t_{12}^{\perp} t_{21}^{\perp}) \cos(\alpha - 2\theta) \\ (\hat{r}_{23}^{\parallel} t_{12}^{\parallel} t_{21}^{\parallel} - \hat{r}_{23}^{\perp} t_{12}^{\perp} t_{21}^{\perp}) \sin \alpha + (\hat{r}_{23}^{\parallel} t_{12}^{\parallel} t_{21}^{\parallel} + \hat{r}_{23}^{\perp} t_{12}^{\perp} t_{21}^{\perp}) \sin(\alpha - 2\theta) \end{pmatrix}. \end{aligned} \quad (4)$$

The effective single-pass propagation length d_{eff} through the sample window is calculated by considering the optical path difference OP between the reference beam and the sample beam, measured from the point of entrance into the sample window to the same phase front of the two output beams. We find that

$$OP = \frac{2n_2 d_{Si}}{\cos \phi'} - d_{air} = \frac{2n_2 d_{Si}}{\cos \phi'} (1 - \sin^2 \phi') = 2n_s d_{Si} \left(1 - \frac{\sin^2 \phi}{n_s^2} \right). \quad (5)$$

Hence we can define

$$d_{eff} = d_{Si} \left(1 - \frac{\sin^2 \phi}{n_s^2} \right). \quad (6)$$

From these general equations it is possible to describe the polarization of the electric field in a wide range of spectrometer geometries. In the following we will investigate the special case $\alpha = 90^\circ$ (vertical input polarization) and an elevation angle $\theta = 60^\circ$. For the purpose of testing the analysis method discussed here, a reflection spectrometer was constructed with these parameters. In this special case, the ratios of the horizontal and vertical components of the electric field reflected from the window-sample interface and the air-window interface, respectively, are

$$\frac{E_{out,x}^{sam}}{E_{out,x}^{ref}} = \frac{\hat{r}_{23,sam}^{\parallel} t_{12}^{\parallel} t_{21}^{\parallel} + \hat{r}_{23,sam}^{\perp} t_{12}^{\perp} t_{21}^{\perp}}{r_{12}^{\parallel} + r_{12}^{\perp}} A_{cal} \exp(i\Delta_{cal}) \exp(2in_2\omega d_{eff}/c) \quad (7)$$

$$\frac{E_{out,y}^{sam}}{E_{out,y}^{ref}} = \frac{\hat{r}_{23,sam}^{\parallel} t_{12}^{\parallel} t_{21}^{\parallel} - 3\hat{r}_{23,sam}^{\perp} t_{12}^{\perp} t_{21}^{\perp}}{r_{12}^{\parallel} - 3r_{12}^{\perp}} A_{cal} \exp(i\Delta_{cal}) \exp(2in_2\omega d_{eff}/c). \quad (8)$$

From this point we will assume that the detector is oriented to detect the x -component of the output field, and drop the subscript x . A typical measurement of the signal trace in this geometry is shown in Fig. 3. The two signals in the trace are the reference signal from the lower interface between air and the silicon window and then, 46 ps later, the sample signal from the reflection at the interface between the silicon window and the sample material, in this case air. This time delay between the reference pulse and the sample pulse is due to the propagation distance of the pulse through the 2.00-mm thick silicon window. The pulses are generated and detected by ultrafast photoconductive switching and sampling, respectively [14]. The temporal separation of the two signals allows an easy separation of the reference and sample signals for the subsequent analysis.

The ratio of the spectra of the sample- and the reference signals is shown in Fig. 4, together with the spectrum of the phase difference between the two signals. The phase difference has been corrected for the accumulated phase due to the propagation distance, $2n_2\omega d_{eff}/c$.

We expect a sign reversal between the two signals since the reference signal is reflected at an interface to a denser medium while the sample signal is reflected at an interface to a less

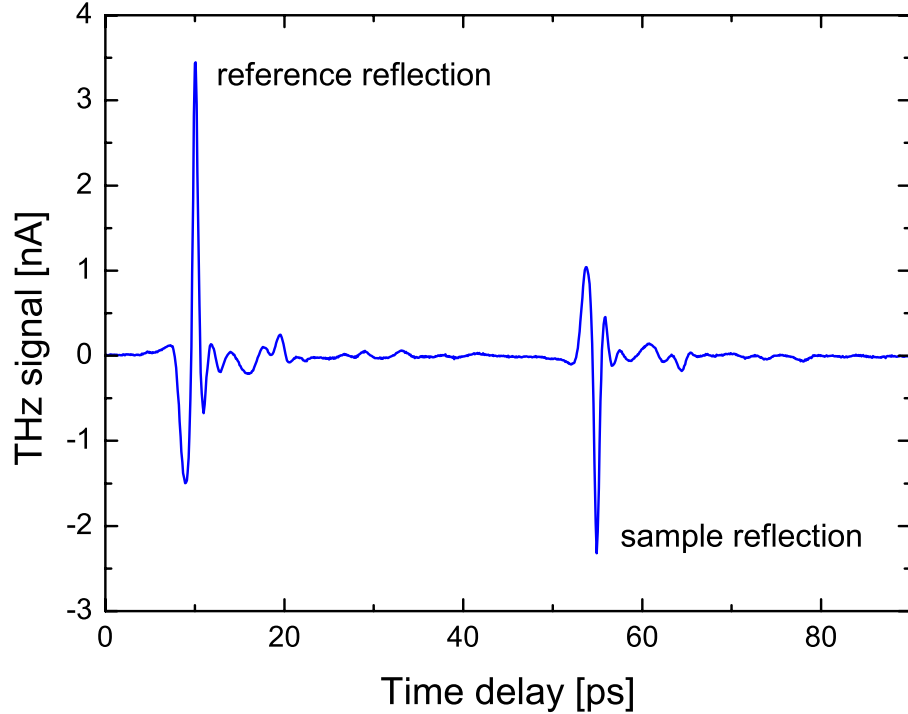


Fig. 3. The THz signal trace recorded in a spectrometer with vertical input polarization ($\alpha = 90^\circ$) and elevation angle $\theta = 60^\circ$. The reference signal is the reflection from the air-silicon interface, and the sample signal is the reflection from the opposite interface between silicon and the sample material, in this case air.

dense medium. This is indicated as the theoretical value π in Fig. 4(b). The measured phase difference is close to this expected value, but nevertheless we observe some differences. The same is the case for the ratio of the amplitudes of the two reflections, shown in Fig. 4(a). The expected ratio of the amplitudes is given by the prefactor in Eq. (7), which has the numerical value 0.697 for our geometry.

The calibration factor $A_{cal} \exp(i\Delta_{cal})$ can be determined by a measurement with air in contact with the window,

$$A_{cal} \exp(i\Delta_{cal}) = \frac{E_{out}^{air}}{E_{out}^{ref}} \frac{r_{12}^{\parallel} + r_{12}^{\perp}}{r_{23,air}^{\parallel} t_{12}^{\parallel} t_{21}^{\parallel} + r_{23,air}^{\perp} t_{12}^{\perp} t_{21}^{\perp}} \exp(-2in_2\omega d_{eff}/c) \quad (9)$$

The amplitude and phase of the calibration factor is shown in Fig. 5. The amplitude of the calibration factor oscillates around unity, and the phase of the calibration factor oscillates around zero. The amplitude of the oscillations indicate that the inclusion of this correction factor in the subsequent analysis is indeed important.

If Eq. (9) is now reinserted into the expression for the sample to reference ratio, now obtained from an unknown sample, one gets

$$A_{sam} \exp(i\Delta_{sam}) \equiv \frac{E_{out}^{sam}}{E_{out}^{ref}} = \frac{\hat{r}_{23,sam}^{\parallel} t_{12}^{\parallel} t_{21}^{\parallel} + \hat{r}_{23,sam}^{\perp} t_{12}^{\perp} t_{21}^{\perp}}{r_{23,air}^{\parallel} t_{12}^{\parallel} t_{21}^{\parallel} + r_{23,air}^{\perp} t_{12}^{\perp} t_{21}^{\perp}} \frac{E_{out}^{air}}{E_{out}^{ref}} \quad (10)$$

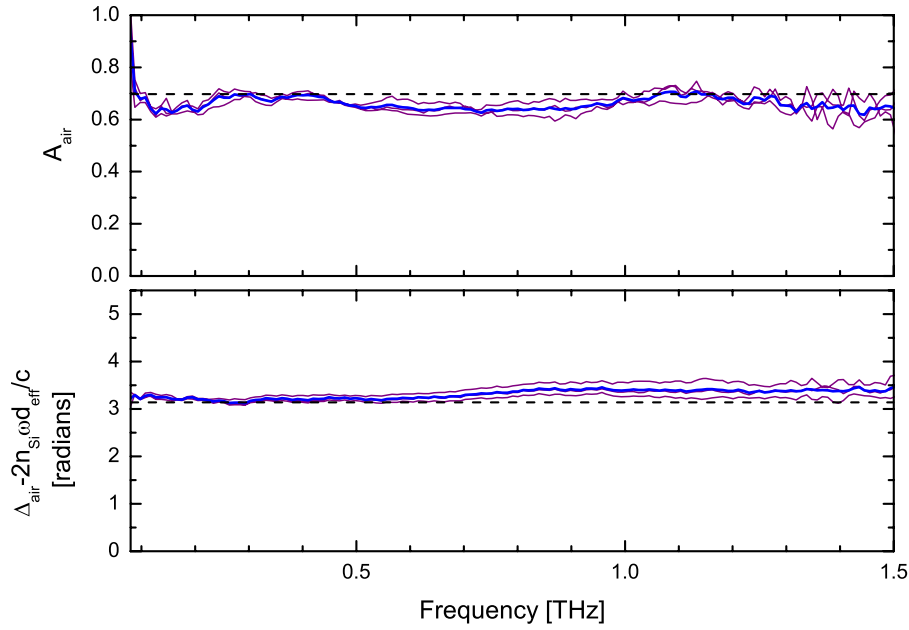


Fig. 4. (a) Amplitude ratio and (b) phase difference between the sample- and reference signal in Fig. 3. The phase difference has been corrected for the accumulated phase due to propagation through the window material. The thin, purple curves show three individual measurements, and the thick, blue curves show the average of these. The dashed lines indicate the theoretical amplitude ratio and phase difference.

The complex index of refraction \hat{n}_3 of the sample material can now be found by solving either Eq. (7) or Eq. (8) with respect to \hat{n}_3 . For this purpose, the functional form of the various reflection- and transmission coefficients must be known. These coefficients are functions of the incidence angle at the respective interfaces. When expressed in terms of the incidence angle $\phi = 90^\circ - \theta$ at the first air-window interface these coefficients can be written as

$$r_{12}^{\parallel} = \frac{-n_2^2 \cos \phi + \sqrt{n_2^2 - \sin^2 \phi}}{n_2^2 \cos \phi + \sqrt{n_2^2 - \sin^2 \phi}}, \quad (11)$$

$$r_{12}^{\perp} = \frac{\cos \phi - \sqrt{n_2^2 - \sin^2 \phi}}{\cos \phi + \sqrt{n_2^2 - \sin^2 \phi}}, \quad (12)$$

$$t_{12}^{\parallel} = \frac{2 \cos \phi}{n_2 \cos \phi + \sqrt{1 - \sin^2 \phi / n_2^2}}, \quad (13)$$

$$t_{12}^{\perp} = \frac{2 \cos \phi}{\cos \phi + n_2 \sqrt{1 - \sin^2 \phi / n_2^2}}, \quad (14)$$

$$t_{21}^{\parallel} = \frac{2n_2 \sqrt{1 - \sin^2 \phi / n_2^2}}{n_2 \cos \phi + \sqrt{1 - \sin^2 \phi / n_2^2}}, \quad (15)$$

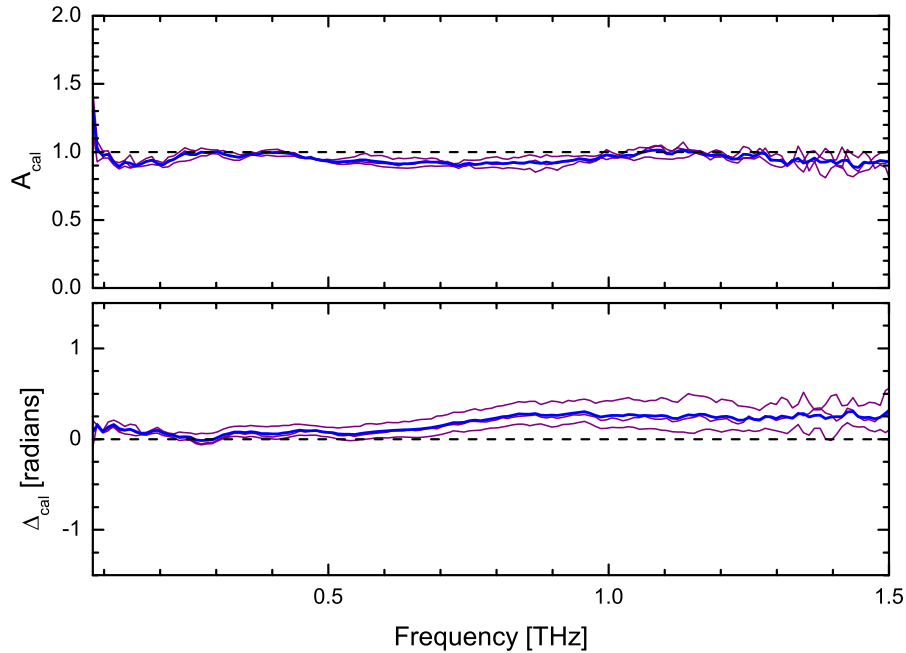


Fig. 5. Amplitude $A(v)$ and phase $\Delta(v)$ of the calibration factor of our spectrometer with $\theta = 60^\circ$ and $\alpha = 90^\circ$ (vertical input polarization). The thin, purple curves show three individual measurements, and the thick, blue curves show the average of these.

$$t_{21}^\perp = \frac{2n_2\sqrt{1 - \sin^2 \phi / n_2^2}}{\cos \phi + n_2\sqrt{1 - \sin^2 \phi / n_2^2}}, \quad (16)$$

$$\hat{r}_{23}^\parallel = \frac{-\hat{n}_3^2\sqrt{n_2^2 - \sin^2 \phi} + n_2^2\sqrt{\hat{n}_3^2 - \sin^2 \phi}}{\hat{n}_3^2\sqrt{n_2^2 - \sin^2 \phi} + n_2^2\sqrt{\hat{n}_3^2 - \sin^2 \phi}}, \quad (17)$$

$$\hat{r}_{23}^\perp = \frac{\sqrt{n_2^2 - \sin^2 \phi} - \sqrt{\hat{n}_3^2 - \sin^2 \phi}}{\sqrt{n_2^2 - \sin^2 \phi} + \sqrt{\hat{n}_3^2 - \sin^2 \phi}}. \quad (18)$$

Inserting these expressions into Eq. (10) results in an expression relating the ratio of the sample- and reference signals and complex index of refraction of the sample material. For a given geometry (incidence angle, window thickness and window refractive index) the sample refractive index is found as the single physically meaningful root of a fourth-order polynomial expression. The solution can be written in closed form if the various coefficients are evaluated numerically for the specific configuration. Due to the complexity of the solution we will not write it out here.

Alternatively the solution can be obtained by an iterative procedure [15], using the values estimated using magic angles (see next section) as initial guess.

The complex index of refraction is related to the dielectric function of the material through the relation $\hat{\epsilon}_3 = \epsilon'_3 + i\epsilon''_3 = \hat{n}_3^2 = (n_3 + i\kappa_3)^2$. In the data analysis in the subsequent sections we will focus on the dielectric function instead of the complex index of refraction.

If we remove the sample material from the silicon window, it is possible to perform an accuracy check of the system. In Fig. 6 we show the resulting apparent real and imaginary part of the dielectric function of air. The real part of the apparent dielectric function of air is located

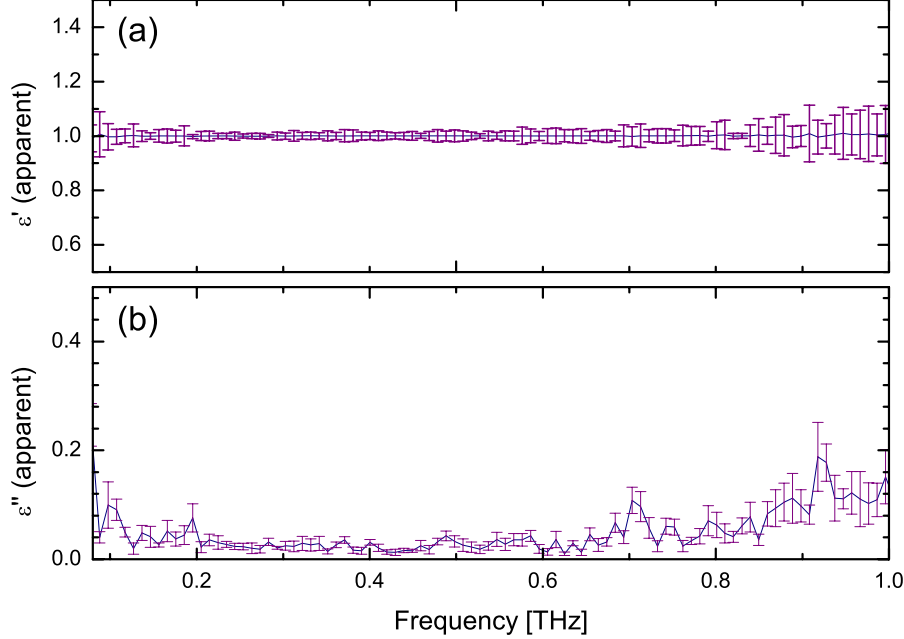


Fig. 6. The apparent (a) real and (b) imaginary part of the dielectric function of air, as measured with the reflection spectrometer. The error bars indicate the standard deviation of the average value of 5 sequential measurements.

very near the expected value $\epsilon'_{air} = 1$, and for low frequencies, the apparent imaginary part of the dielectric function of air, ϵ''_{air} , is close to zero, as expected. However, ϵ''_{air} increases slightly at higher frequencies. This increase is caused by small uncertainties in the detected phase of the sample signal, compared to the reference measurement. This source of error seems to be most important for samples with a very small absorption, as will be discussed in Section 2.3.

2.2. Analysis using magic angles

The complexity of the analysis arises from the presence of both *s*- and *p*-polarized light at the sample interface. For a given elevation angle θ , a pure *s*- or *p*-polarization at the sample interface can be obtained by appropriate rotation of the input polarization ($\alpha = 60^\circ$ gives pure *s*-polarization and $\alpha = -30^\circ$ gives pure *p*-polarization). In these cases the extraction of the complex index of refraction of the sample material becomes significantly simpler than for the situation where both *s*- and *p*-components are present at the reflection.

For an incident polarization angle of $\alpha = 60^\circ$ the ratio of the *x*- and *y*-projections of the output field are identical, and can be expressed as of the sample and reference signals are

$$A_{sam}^\perp \exp(i\Delta_{sam}^\perp) = \frac{\hat{r}_{23,sam}^\perp}{r_{23,air}^\perp} \frac{E_{out}^{air}}{E_{out}^{ref}} . \quad (19)$$

Correspondingly, for $\alpha = -30^\circ$, the ratio of the *x*- and *y*-components of the output field are

identical, and can be expressed as

$$A_{sam}^{\parallel} \exp(i\Delta_{sam}^{\parallel}) = \frac{\hat{r}_{23,sam}^{\parallel}}{r_{23,air}^{\parallel}} \frac{E_{out}^{air}}{E_{out}^{ref}} . \quad (20)$$

Although the *ratio* of the *x*- and *y*-components of the output field are the same in these expressions, the *overall* signal strength, and consequently also the signal-to-noise ratio, can be optimized by aligning the polarization axis of the detector with the polarization of the output field.

As an example, if the emitter is mounted so that it results in an input polarization $\alpha = 60^\circ$, the complex index of refraction of the sample material can be found to be

$$\hat{n}_{sam} = \frac{\sqrt{(1 - \hat{r}_{23,sam})^2 n_2^2 + 4\hat{r}_{23,sam} \sin^2 \phi}}{1 + \hat{r}_{23,sam}} , \quad (21)$$

where $\hat{r}_{23,sam}$ is found by inverting Eq. (19). The imaginary part of the index of refraction (the extinction coefficient) is related to the absorption coefficient, $\hat{n}_{23,sam} = n + i\kappa = n + i\alpha c/2\omega$.

2.3. Verification of the accuracy of the spectrometer

In the next section we will describe an application of the reflection spectrometer. In order to verify the accuracy of the analysis method described in the previous sections, we performed a calibration measurement with deionized water and pure ethanol as sample materials. The spectrometer was set up with the input polarization $\alpha = 90^\circ$ and elevation angle $\theta = 60^\circ$, and hence the full analysis with mixed polarization at the sample interface has been applied.

In order to compare our results with already published data the dielectric functions measured for water and ethanol, respectively, are shown in Fig. 7. The real and imaginary part of the dielectric function are defined as $\epsilon' + i\epsilon'' = (n + i\kappa)^2$. The dielectric spectrum of water has been analyzed applying the double Debye model with two relaxation times [10, 11, 2],

$$\epsilon(\omega) = \frac{\epsilon_s - \epsilon_1}{1 - i\omega\tau_1} + \frac{\epsilon_1 - \epsilon_\infty}{1 - i\omega\tau_2} + \epsilon_\infty . \quad (22)$$

Likewise, the dielectric spectrum of ethanol has previously been analyzed using the triple Debye model [10, 11],

$$\epsilon(\omega) = \frac{\epsilon_s - \epsilon_1}{1 - i\omega\tau_1} + \frac{\epsilon_1 - \epsilon_2}{1 - i\omega\tau_2} + \frac{\epsilon_2 - \epsilon_\infty}{1 - i\omega\tau_3} + \epsilon_\infty , \quad (23)$$

where three relaxation times are required for a satisfactory agreement between experimental data and the model. In Table 1 we compare the fitting parameters obtained using our data and data from the literature [10, 11, 2].

In our analysis of the water dielectric spectrum we have kept the value of the static permittivity ϵ_s constant at the value determined in microwave experiments by Barthel *et al.* [10]. Because of the rapid increase of the dielectric function at low frequencies we cannot reliably fit the value of ϵ_s from our experimental data. Similarly, during the fitting of the triple Debye model to our experimental ethanol data, we kept the values of ϵ_s , ϵ_1 , and τ_1 fixed at the values reported by Barthel *et al.* [10].

The good agreement between the result of our analysis and published values of the Debye parameters confirms that the spectrometer configuration in reflection geometry with both *s*- and *p*-polarized THz light incident on the sample window at non-normal incidence, together with the analysis outlined above, can precisely characterize the dielectric properties of liquids.

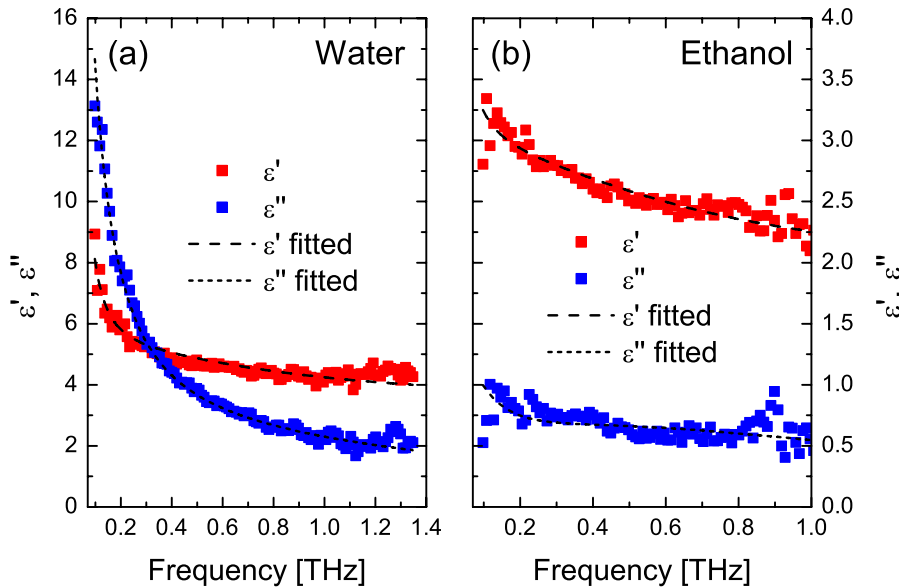


Fig. 7. The real (red symbols) and imaginary (blue symbols) part of the dielectric function of (a) water and (b) ethanol recorded at a temperature of 20°C. The fitted curves are described in the text.

3. Reflection spectroscopy of ethanol-water solutions

The analysis outlined in the previous sections will now be applied to spectroscopy of aqueous solutions of ethanol and sucrose. The results in Fig. 7 demonstrate the significant difference in the dielectric properties of pure water and pure ethanol in the THz range. Kitahara *et al.* used transmission THz-TDS to determine the dielectric function of water-ethanol mixtures [12]. Recently, Nagel *et al.* used a corrugated parallel-plate waveguide chip to measure the real and imaginary parts of the refractive index in water-ethanol mixtures [13].

We prepared a series of 21 samples of water-ethanol mixtures with varying alcohol content from 0% to 100%, increased in 5%-steps. Each of these samples were then characterized with our reflection setup. The temperature of the sample material was determined by the ambient temperature of the laboratory, and remained stable within 1-2 Kelvin during the measurements. The real and imaginary parts (in the following denoted ϵ' and ϵ'' , respectively) of the dielectric function in the frequency range 0.1-1.1 THz of these mixtures are shown in Fig. 8.

Both ϵ' and ϵ'' show a pronounced dependence on the alcohol concentration. The effect is strongest on ϵ'' . We also note the gradual and monotonic change of the dielectric function from that of pure water to that of pure ethanol, in agreement with the dielectric spectra based on transmission measurements reported by Kitahara *et al.* [12].

The pronounced dependence of ϵ' and ϵ'' on the alcohol concentration suggests that we can determine the alcohol concentration of an aqueous solution of alcohol by comparing the dielectric function of the unknown sample to the reference curves in Fig. 8. Chemometric approaches such as principal components analysis would be a standard method for this determination. However, due to the lack of distinct spectral features only a single, or at most two, principal components of the spectra will contain useful information. Therefore we will apply a simpler approach, with basically the same accuracy. In Fig. 9 we have plotted the average value over the frequency range 0.15-1.0 THz of ϵ' and ϵ'' , as functions of the ethanol concentration

Table 1. Comparison with existing literature of Debye model parameters for water and ethanol. Values marked with $*$ have been kept fixed in the fitting process. The reported uncertainties are the standard deviations of the estimated parameter values.

Water, double Debye model parameters

	This work	Kindt <i>et al.</i> [11]	Rønne <i>et al.</i> [2]	Barthel <i>et al.</i> [10]
ϵ_s	78.36*	78.36*	80.58*	78.36
τ_1 [ps]	7.89 ± 0.06	8.24 ± 0.40	8.5 ± 0.4	8.32
ϵ_1	5.16 ± 0.06	4.93 ± 0.54	5.2 ± 0.1	6.18
τ_2 [ps]	0.181 ± 0.014	0.180 ± 0.014	0.170 ± 0.04	1.02
ϵ_∞	3.49 ± 0.07	3.48 ± 0.70	3.3 ± 0.3	4.49

Ethanol, triple Debye model parameters

	This work	Kindt <i>et al.</i> [11]	Barthel <i>et al.</i> [10]
ϵ_s	24.35*	24.35*	24.35
τ_1 [ps]	163*	161	163
ϵ_1	4.49*	4.15	4.49
τ_2 [ps]	3.01 ± 0.21	3.3	8.97
ϵ_2	2.91 ± 0.04	2.72	3.82
τ_3 [ps]	0.235 ± 0.018	0.22	1.81
ϵ_∞	1.949 ± 0.034	1.93	2.29

in the solution.

The solid curves are phenomenological fits to the average values of ϵ' and ϵ'' , in the following denoted $\bar{\epsilon}'$ and $\bar{\epsilon}''$ in the frequency range 0.15-1.0 THz. We used an exponential function to fit both curves,

$$\bar{\epsilon}'(x) = A' + B' \exp(-C'x), \quad (24)$$

$$\bar{\epsilon}''(x) = A'' + B'' \exp(-C''x), \quad (25)$$

with the fitting parameters $A' = 0.137$ (kept fixed), $B' = 4.554 \pm 0.029$, $C' = 0.623 \pm 0.013$, $A'' = 0.501 \pm 0.052$, $B'' = 3.534 \pm 0.053$, and $C'' = 3.177 \pm 0.14$, obtained by a standard non-linear least-squares curve fitting routine.

In the case of ideal additivity of the contributions to the total optical attenuation and dispersion from the two components of the mixture, we expect [16, 18, 19] the complex index of refraction to be of the form

$$\hat{n}_{ideal}(v) = \frac{c_{H_2O}^{mix}}{c_{H_2O}^{neat}} \hat{n}_{H_2O}(v) + \frac{c_{EtOH}^{mix}}{c_{EtOH}^{neat}} \hat{n}_{EtOH}(v), \quad (26)$$

where c_i^{mix} is the concentration of component i in the mixture and c_i^{neat} is the concentration of the component i in a neat sample of the component. The dashed lines in Fig. 9 shows the ideal behavior of the average dielectric function of the mixtures. These curves were calculated by using the absorption coefficient and index of refraction of neat water and neat ethanol, respectively, to calculate the effective complex index of refraction $\hat{n}_{ideal}(v)$ for each mixing ratio,

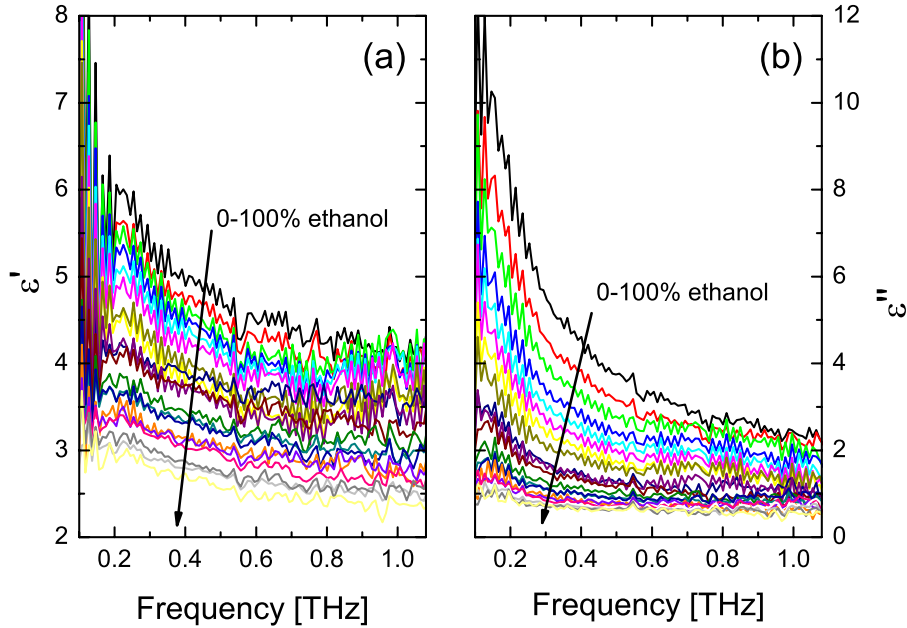


Fig. 8. The (a) real and (b) imaginary part of the dielectric function at room temperature of water-ethanol mixtures in the 0.1-1.1 THz range. The alcohol concentration is varied from 0% to 100% in 5%-steps.

using Eq. (26). Subsequently the dielectric function $\bar{\epsilon}'_{ideal}(x)$ and hence $\bar{\epsilon}''_{ideal}(x)$ could be calculated.

The observed behavior of both $\bar{\epsilon}'$ and $\bar{\epsilon}''$ is markedly different from the ideal mixing behavior. we observe that both $\bar{\epsilon}'$ and $\bar{\epsilon}''$ are smaller than expected from the ideal additivity hypothesis.

In a infrared study of mixtures of benzene and fluorinated benzene [16], Tassaing *et al.* concluded that only insignificant deviation from the additivity hypothesis was observed, although the authors mention a deviation below 30 cm^{-1} . Flanders *et al.* [17] studied mixtures of CHCl_3 and CCl_4 , and found an increasing deviation from the ideal mixing behavior with increasing polar nature of the mixture. Venables *et al.* discussed mixtures of acetone/methanol, acetone/acetonitrile, and methanol/acetonitrile [18] and saw small deviations from the ideal additivity only in acetone/acetonitrile mixtures. In another study, Venables and Schmuttenmaer observed significant deviations from ideal additivity in water/acetone, water/acetonitrile, and water/methanol mixtures [19], specifically with a lower absorption coefficient and index of refraction of the mixture than expected for a mixture showing ideal additivity. Our observation of non-ideal mixing behaviour in a mixture of polar liquids is hence in agreement with the trend of already published observations.

If an unknown solution of ethanol in water is characterized by our setup, we can in a similar fashion determine $\bar{\epsilon}'$ and $\bar{\epsilon}''$. Inverting Eqs. (24) and (25) and forming the average of the two determinations of x , results in an estimate of the alcohol concentration of the unknown solution. This procedure was carried out on samples with ethanol concentrations from 0% to 100%, resulting in the correlation diagram shown in Fig. 10. The estimated alcohol concentration of the 21 samples with pure water and pure ethanol is shown as black symbols. The error bars are the standard deviations of each estimate, determined by the standard deviations of the fitted constants in Eqs. (24) and (25) as well as the standard deviations of $\bar{\epsilon}'$ and $\bar{\epsilon}''$ of the sample.

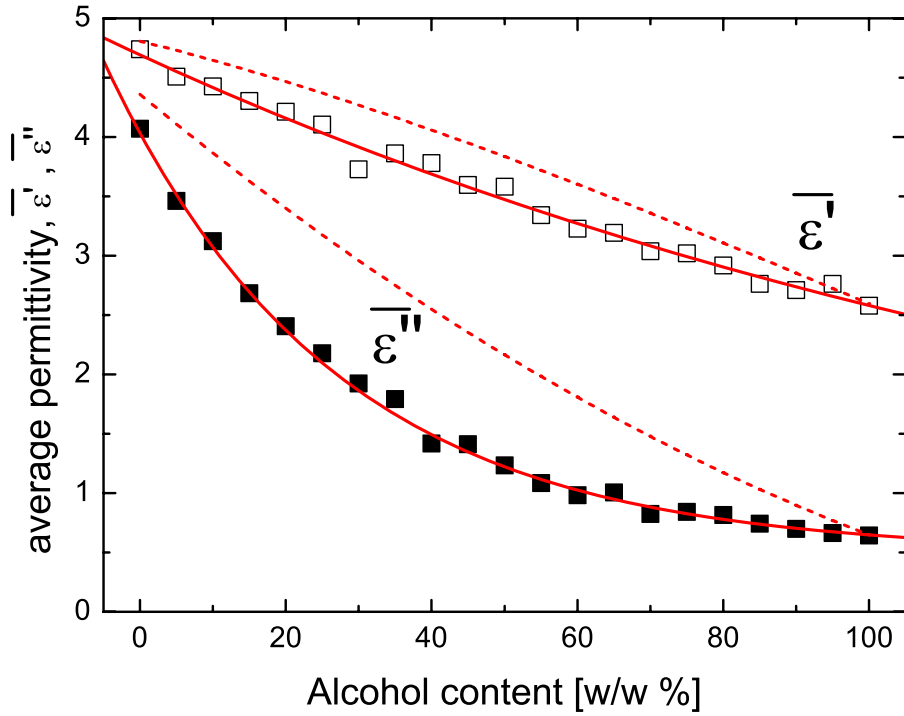


Fig. 9. The average value of the real and imaginary part of the dielectric function of water-ethanol mixtures in the 0.15-1.0 THz range, as function of the ethanol concentration. Solid curves are phenomenological fits to the experimental data, and the dashed lines show the ideal behavior of the mixtures.

The correlation between the reported and the estimated alcohol concentration is close to unity, with a slope of the best fit through the origin of 0.998. The standard deviation of the estimated values is approximately 1% at low alcohol concentrations, but increase to several % at higher concentrations. This is due to the decreasing slope of Eq. (25) at high alcohol concentrations.

Also shown in Fig. 10 are the estimated alcohol concentrations of a selection of commercial beverages and liquors, with alcohol strengths, converted from the labeling of the bottle to weight percentage, of 0.1% (alcohol-free beer), 4% (Danish Pilsner), 6.1% (Danish Porter beer), 8.8% (French white wine), 13.7% (Irish cream liquor), 37% (German Bitter), and 52% (Bulgarian Absinthe). The blue star-shaped symbols show the estimated concentrations versus the concentrations according to the labeling.

The estimated alcohol concentrations of the commercial alcohols are predicted with an accuracy of better than 1% with respect to the labeled alcohol strength, with the notable exception of the cream liquor. However, for this special liquor this strong deviation is to be expected since the content of cream leads to a significant reduction of both $\overline{\epsilon}'$ and $\overline{\epsilon}''$. Hence the initial assumption, that only alcohol contributes to the reduction of $\overline{\epsilon}'$ and $\overline{\epsilon}''$ is not valid for this type of liquor.

3.1. Influence of carbonation and sugar

It could be expected that measurements on carbonated solutions, such as softdrinks and sparkling wines, would be a special challenge for an optical detection technique. Transmis-

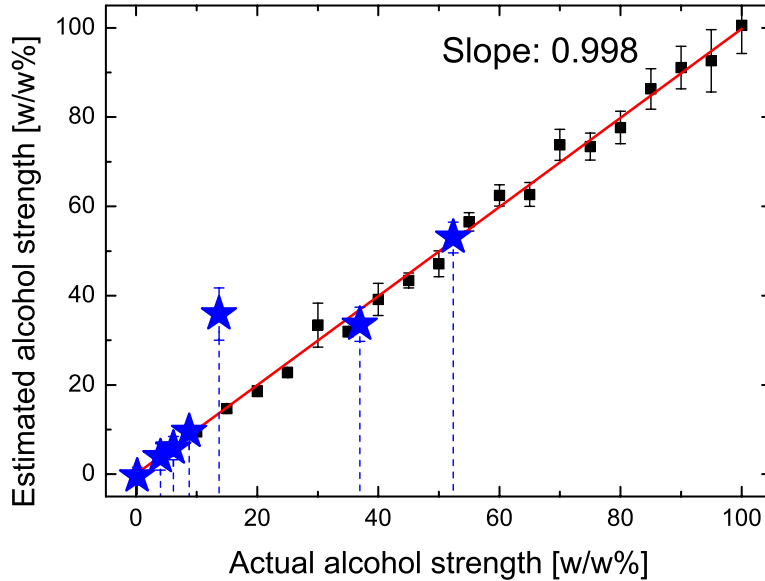


Fig. 10. The correlation between the known and the predicted concentration of ethanol in mixtures of deionized water and ethanol (black symbols) and commercial alcoholic beverages and liquors (blue, star-shaped symbols).

sion measurements would indeed be influenced by the presence of gas bubbles in the liquid due to strong and random scattering of the light on the bubbles.

The special configuration of the sample window, where the interface between the window and the liquid is oriented horizontally, allows bubbles formed in the sample liquid to rapidly escape the interface region. Hence carbonated liquids can be characterized with virtually the same accuracy as still samples. This is demonstrated in Fig. 11(a), where the dielectric function of pure water (black curve) is compared to that of carbonated mineral water (red curve) and the same carbonated water with the gas removed by vigorous shaking of the bottle prior to the measurements (blue curve). During the measurement on the carbonated water sample the formation and release of numerous gas bubbles was clearly visible.

The close resemblance of the spectra in Fig. 11 shows that the influence of carbonation on the reflection measurement of the dielectric properties is minimal. The reason why the influence on the measurements is so small is most likely that the time from formation of the gas bubble to its release from the interface is very short compared to the measurement time. At the same time, the large area of the sample interface reduces the probability that the gas bubbles are formed at the area sampled by the THz beam.

A closer look at Fig. 11(a) reveals that the real part of the dielectric function of the carbonated water is slightly larger than that of deionized water. Since this slight increase of $\bar{\epsilon}^r$ is the same for carbonated and decarbonated water, we rule out the formation of bubbles at the sample interface as the cause of this increase. More likely, the temperature of the sample material has varied slightly between the time of the measurement of the deionized water and the time of the

measurement of the carbonated and decarbonated water. The temperature is known to have a pronounced effect on the dielectric function of water in the THz range [2].

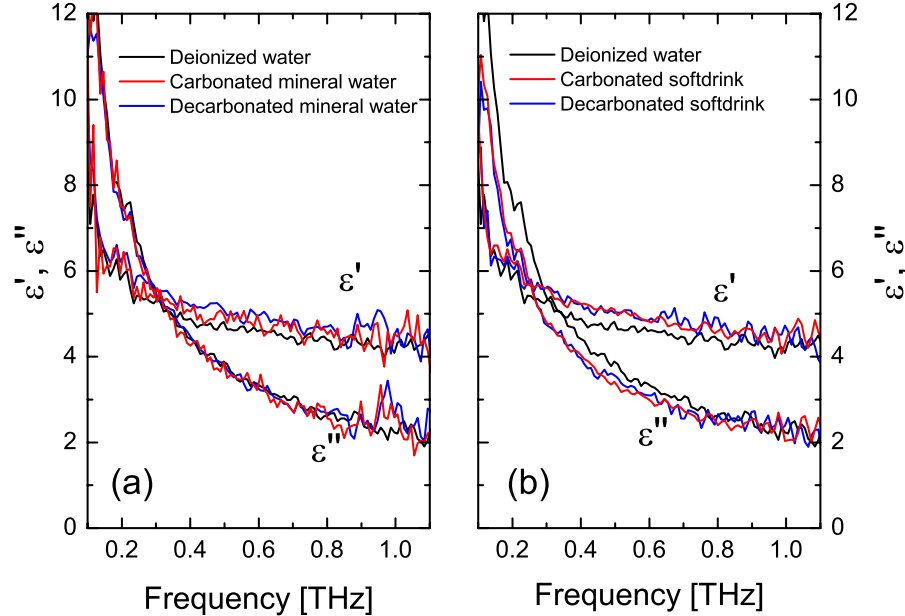


Fig. 11. The real and imaginary part of the dielectric function at room temperature of (a) deionized water, carbonated mineral water, and mineral water with gas removed, and (b) deionized water, a typical carbonated softdrink, and the same softdrink with the gas removed.

We repeated the measurements on various brands of carbonated water, and found that there is no significant and reproducible difference between the dielectric functions of the carbonated water and that of deionized water.

The influence of the sugar content in a commercial, carbonated softdrink on the dielectric function is investigated in Fig. 11(b). Here the dielectric function of the carbonated softdrink (red curve) and the same softdrink with the gas removed (blue curve), again by vigorous shaking of the bottle prior to the measurement, are shown. Again the formation of bubbles at the interface to the sample window seems to have minimal influence on the measurement. However, the real part of the dielectric function of the softdrink is higher than that of deionized water (black curve), and the imaginary part of the dielectric function is lower than that of deionized water, especially at frequencies below 0.7 THz. This difference can be attributed to the sugar content of the softdrink. In Fig. 12 we show the dielectric function of aqueous solutions of sucrose, for sucrose concentrations between 0 and 75% by weight. Preparation of the highest concentrations required a slight heating of the solution in order to dissolve the sucrose, but all measurements are carried out with the sample material at room temperature and without precipitation of sucrose crystals.

The real part of the dielectric function of aqueous solutions of sucrose shows only a weak dependence on the sucrose concentration. The imaginary part of the dielectric function, however, displays a significant dependence on the sucrose concentration. This is in contrast to the effect of mixing ethanol and water, where a pronounced dependence on the ethanol concentration was observed in both the real and imaginary part of the dielectric function of the solution.

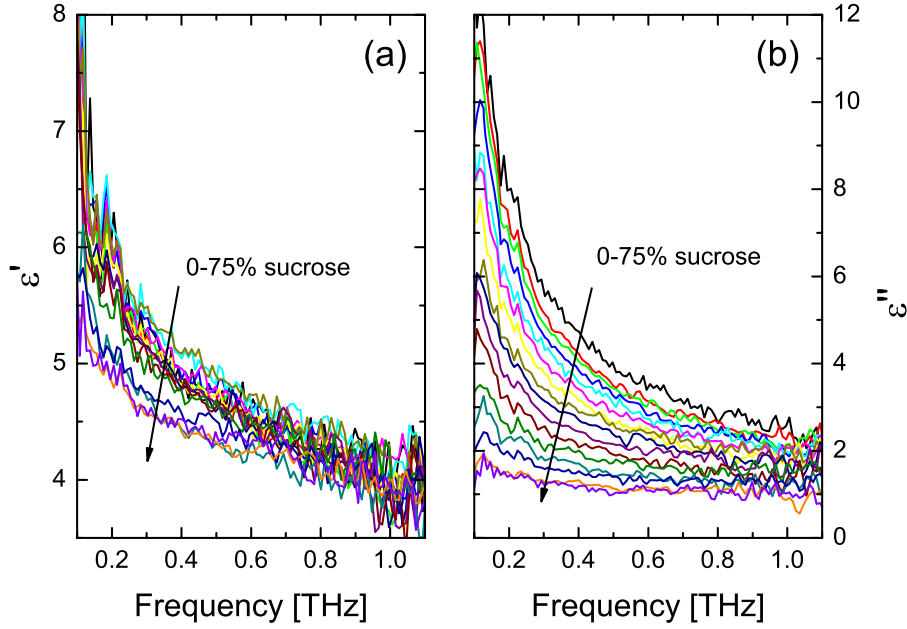


Fig. 12. The real and imaginary part of the dielectric function at room temperature of aqueous sucrose solutions, with sucrose concentrations from 0% to 75% by weight, measured in 5%-intervals.

The dependence on sucrose concentration of the average dielectric function in the frequency range 0.15-1.0 THz of the sucrose solutions is shown in Fig. 13.

The real part of the dielectric function of the sucrose solutions is seen to be basically independent of the sucrose concentration up to concentrations of approximately 40% by weight. At higher concentrations, a slight decrease of ϵ' is observed. The same plot shows a linear decrease of ϵ'' with increasing sucrose concentration. The red curves in Fig. 13 are linear fits to the data, using the functions

$$\epsilon'(y) = \begin{cases} D', & y < 40\% \\ -E'y + F', & y \geq 40\% \end{cases} \quad (27)$$

$$\epsilon''(y) = -E''y + F'' \quad (28)$$

with the fitting parameters $D' = 4.763 \pm 0.032$, $E' = 5.05 \pm 0.14$, $F' = 0.00978 \pm 0.0024$, $E'' = 0.0415 \pm 0.0007$, and $F'' = 4.11 \pm 0.03$.

3.2. Simultaneous determination of alcohol and sugar concentration

Having demonstrated that the dielectric function of an aqueous solution is sensitive both to the ethanol content and to the sucrose content we will now investigate if the technique can be used for the *simultaneous* determination of the concentration of both these components in an aqueous solution. The basis for this approach is that the modification of the dielectric function of the solution can be described as a sum of the individual modifications arising from the alcohol content and from the sugar content. Clearly this is an assumption that may only hold over a limited range of concentrations of alcohol and sugar. However, most commercial beverages and liquors contain a relatively small concentration of sugar.

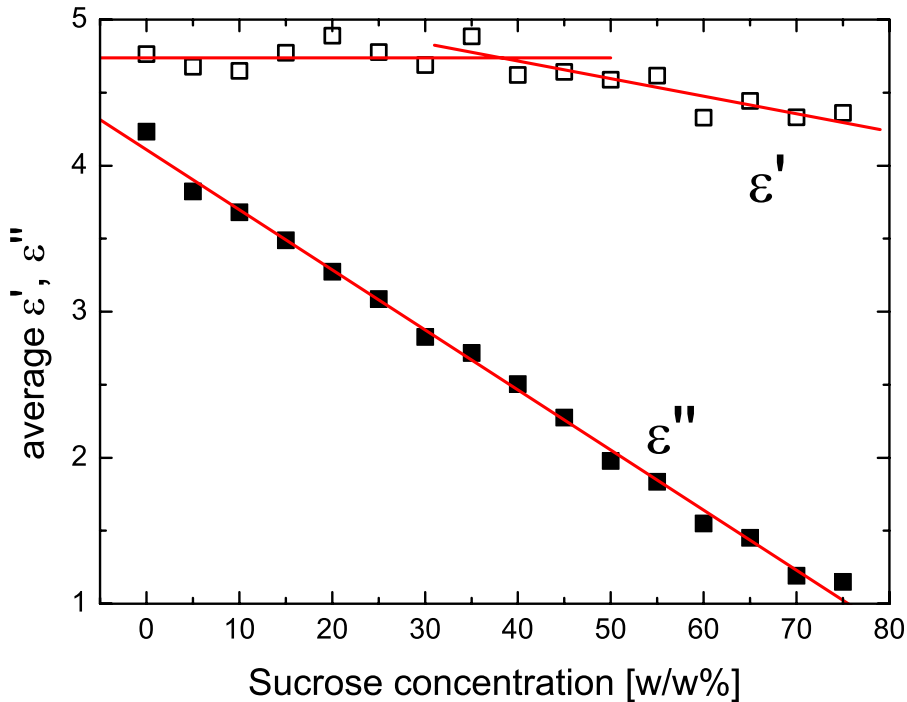


Fig. 13. The average value of the real and imaginary part of the dielectric function in the frequency interval 0.15-1.0 THz of aqueous sucrose solutions as function of the sucrose concentration. The solid curves are phenomenological fits, as discussed in the text.

In Fig. 14 the real and imaginary part of the dielectric function for mixtures of sucrose and ethanol in water are shown together with the dielectric functions of pure water, a water-ethanol solution, and a water-sucrose solution. Clearly the addition of up to 20% sucrose to the pure water as well as to the alcohol solution has little effect on the real part of the dielectric function of the solution. The effect of adding 10 and 20% sucrose to the solutions is however clearly seen in the lowering of the imaginary part of the dielectric function of the solution.

If we denote the ethanol concentration x and the sucrose concentration y , the above analysis indicates that the average dielectric function in the frequency interval 0.15-1.0 THz of a solution of ethanol and sugar in water can be written as

$$\epsilon'(x,y) = A' + B' \exp(-C' x) \quad (29)$$

$$\epsilon''(x,y) = A'' + B'' \exp(-C'' x) - E'' y \quad (30)$$

where the constants in these equations are the same as given earlier. When using this analysis on the dielectric functions of the sucrose-ethanol solutions in Fig. 14 we obtain a fairly good agreement between the known concentrations of sucrose and ethanol and the concentrations predicted by the model. Specifically, the 10%-sucrose-20%-ethanol solution was predicted to contain $(13.6 \pm 2.5)\%$ sucrose and $(18.6 \pm 1.1)\%$ ethanol. The 20%-sucrose-20%-ethanol solution was predicted to contain $(19.4 \pm 2.5)\%$ sucrose and $(19.4 \pm 1.1)\%$ ethanol.

The extraction of the concentration of two components in the solution is possible because we measure both the real and imaginary part of the dielectric function. Two components is the

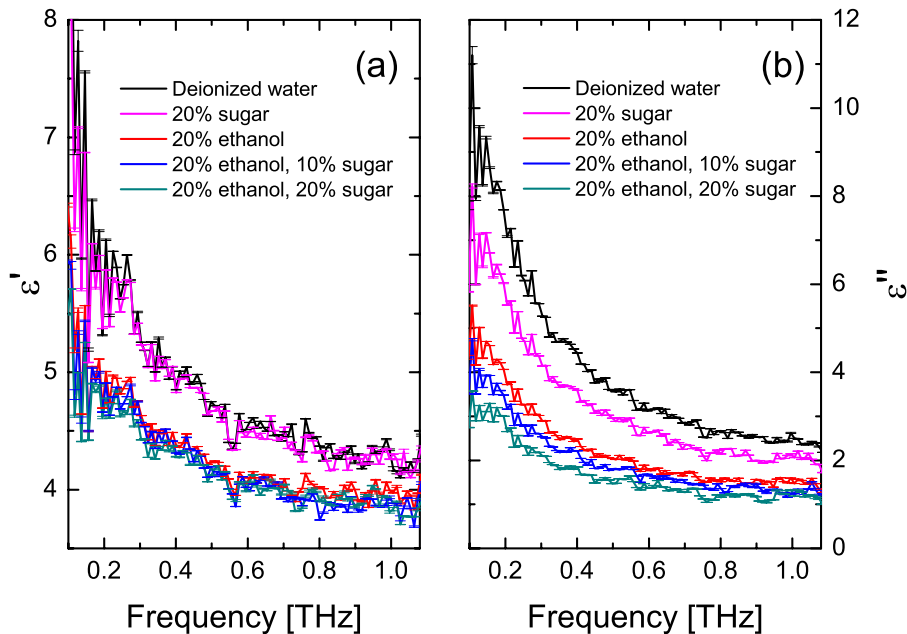


Fig. 14. The real and imaginary part of the dielectric function of pure water, a 20% sucrose solution, a 20% ethanol solution, and two solutions containing 10 and 20% sucrose and 20% ethanol.

maximum number of components that can be quantified with the method applied here, and the method requires that (a) no other components in the liquid contributes significantly to changes of the dielectric function of the solvent (here water) and (b) that changes of the dielectric function owing to the presence of two components can be described as the sum of the individual contributions. The quantification of even more complex mixtures of components would require specific signatures in the dielectric spectrum. The presence of such signatures would effectively increase the dimensionality of the data set, and chemometric approaches would become efficient. We have carried out a rigorous principal components analysis on the data presented here and found that the lack of distinct spectral features in the dielectric functions resulted in the same accuracy as the method applied above.

4. Conclusions

We have analyzed a method for the extraction of the dielectric function of a sample in the THz region by self-referenced reflection THz time-domain spectroscopy. The analysis takes an arbitrary incidence angle, as well as arbitrary input polarization of the THz field into account, and we validated the data extraction procedure in a comparison between our measurement of the dielectric functions of liquid water and ethanol and reported data in the literature.

We then devised a method for the determination of the alcohol content in water-alcohol mixtures, based on the THz dielectric properties of the mixture. Interestingly, this method can also be used to determine the alcohol concentration in commercial beverages and liquors. The accuracy of the method was found to be highest at low alcohol concentrations. The accuracy is mainly determined by the signal-to-noise level of the spectrometer.

The simultaneous measurement of both the real and the imaginary part of the dielectric func-

tion gives the possibility of determination of two ingredients in an aqueous solution, even in the absence of spectral features in the dielectric function of the sample. We demonstrated that it is possible to determine both alcohol and sugar content with an accuracy of a few percent in the concentration range typically found in commercial beverages and liquors.

We expect that stabilization of the sample temperature will further increase the accuracy of the method, making the method interesting for commercial applications.

This work was supported in part by the Danish Natural Science Research Council and the EU Integrated Project TeraNova.